The Cryosphere Discuss., 9, 5253–5289, 2015
www.the-cryosphere-discuss.net/9/5253/2015/
doi:10.5194/tcd-9-5253-2015

The Cryosphere Discussions
Open Access

Tremor during ice stream stick-slip

B. P. Lipovsky[1] **and E. M. Dunham**[1,2]

[1]Department Geophysics, Stanford University, Stanford, CA, USA
[2]Institute for Computational and Mathematical Engineering, Stanford University, Stanford, CA, USA

Received: 1 September 2015 – Accepted: 12 September 2015 – Published: 30 September 2015

Correspondence to: B. P. Lipovsky (lipovsky@stanford.edu)

Published by Copernicus Publications on behalf of the European Geosciences Union.

Abstract

During the 200 km-scale stick slip of the Whillans Ice Plain (WIP), West Antarctica, seismic tremor episodes occur at the ice–bed interface. We interpret these tremor episodes as swarms of small repeating earthquakes. The earthquakes are evenly spaced in time and this even spacing gives rise to spectral peaks at integer multiples of the recurrence frequency ∼ 10–20 Hz. We conduct numerical simulations of the tremor episodes that include the balance of forces acting on the fault, the evolution of rate- and state-dependent fault friction, and wave propagation from the fault patch to a seismometer located on the ice. The ice slides as an elastic block loaded by the push of the upstream ice, and so the simulated basal fault patch experiences a loading velocity equal to the velocity observed by GPS receivers on the surface of the WIP. By matching synthetic seismograms to observed seismograms, we infer fault area $\sim 10\,m^2$, bed shear modulus ∼ 10 MPa, effective pressure ∼ 10 kPa, and state evolution distance ∼ 1 µm. Large-scale slip events often occur twice daily, although skipped events have been increasing in frequency over the last decade. We observe that tremor seismic particle velocity amplitudes are greater during the double wait time events that follow skipped events. The physical mechanism responsible for these anomalously high seismic amplitudes may provide a window into near-future subglacial conditions and the processes that occur during ice stream stagnation.

1 Introduction

Concern about future sea level rise motivates a study of the subglacial conditions that give rise to streaming ice (Joughin and Alley, 2011). The Whillans Ice Plain (WIP) region of the West Antarctic Ice Sheet (WAIS) is notable for decelerating from previously fast streaming flow over the instrumental record (Beem et al., 2014). Since most ice flux in Antarctica occurs through ice streams (Whillans et al., 1987; Rignot et al., 2011), understanding the conditions that cause ice stream stagnation is of basic im-

TCD
9, 5253–5289, 2015

portance in constraining the continent's contribution to future sea level rise. Although recent progress has been made in describing the relationship between basal conditions and ice stream motion (Bougamont et al., 2011; Robel et al., 2013; Kyrke-Smith et al., 2014, 2015), direct observation of the temporal variation in subglacial conditions during ice stream stagnation has remained elusive.

Antarctic ice streams exhibit a wide variety of stick-slip behavior. The WIP is an extreme case wherein the entire $\sim 2 \times 10^4$ km^2 ice plain undergoes tidally-modulated once- or twice-daily stick-slip motions (Bindschadler et al., 2003; Wiens et al., 2008). During the time between large-scale sliding events, several ~ 100 km^2 regions exhibit a high degree of locking (Winberry et al., 2014c). Slip motion observed by on-ice GPS instruments then begins within the locked region and propagates outward towards the ice stream margins and grounding zone (Pratt et al., 2014).

The focus of our study is a type of seismic tremor first identified by Winberry et al. (2013) that occurs during large-scale slip motion. We follow Winberry et al. (2013) in attributing these tremor episodes to small repeating earthquakes at the bed of the WIP (Fig. 2 and Sect. 3). The earthquakes are evenly spaced in time and this even spacing gives rise to spectral peaks that are inversely proportional to the earthquake recurrence time (Fig. 3d) (Powell and Neuberg, 2003; MacAyeal et al., 2008). Over the 30 min duration of a tremor episode, the earthquake recurrence time gradually changes, causing the spectral peaks to glide (Fig. 3a).

The goal of this study is to quantitatively describe the relationship between conditions at the bed of WIP and the tremor that occurs there. To do this, we simulate the evolution of elastic and frictional forces along a small fault patch at the boundary between ice and bed (Sect. 5). Rapid motion along the fault excites waves that are recorded at a seismometer, and we account for this wave propagation. The simulated tremor-producing fault patch is loaded with surface velocity data recorded using GPS stations on the WIP.

A basic question is whether the events occur at an ice-ice, ice-till or ice–bedrock interface. An observation of fundamental importance in this regard is that observed

TCD
9, 5253–5289, 2015

seismic particle velocity amplitudes are $\sim 100\,\mathrm{nm\,s^{-1}}$. Low seismic amplitudes could exist for a number of reasons. We attribute low seismic amplitudes to a bimaterial effect: when seismic slip occurs at an interface between a rigid and a compliant material, more motion occurs in the compliant material. All else being equal, low amplitudes are therefore support for a highly compliant bed material.

We observe a previously undocumented phenomenon: tremor seismic amplitudes are anomalously high during large-scale slip events that follow a skipped slip event. We refer to such large scale slip events as double wait time events. In Sect. 7, we propose two distinct mechanisms to account for the observed anomalous seismic amplitudes: stiffening of the bed and reduction of aseismic slip. Double wait time events have been becoming more frequent in the last decade (Winberry et al., 2014c). The physical conditions that result in elevated seismic amplitudes during tremor may therefore be related to the conditions that will prevail in the near-future if stagnation continues.

2 Observations

We examine collocated seismic and geodetic data collected at the WIP during field seasons in 2010–2011 and 2011–2012 (Fig. 1) (Winberry et al., 2014a, b). The GPS-measured ice surface position was recorded at 15 s intervals. During large-scale sliding events, the ice surface velocity reaches an elevated value and then gradually decays over a period of about 15 min (Fig. 4a). The data in Fig. 4 are aligned so that $t = 0$ corresponds to the time of maximum sliding velocity for each event. The fastest recorded velocity observed during any of the sliding events in our data set is $7.47 \times 10^{-4}\,\mathrm{m\,s^{-1}}$ or $64.5\,\mathrm{m\,day^{-1}}$. We low pass filter all GPS data below 500 s.

Large-scale sliding events are observed either one or two times per day. The timing of these events is nearly synchronous with the high and low ocean tides (Bindschadler et al., 2003). When a high or low tide occurs without a sliding event, the next event to occur is termed a double wait time event. Double wait time events have unique properties that we describe in Sect. 7.

TCD
9, 5253–5289, 2015

During large-scale sliding events, several seismometers record tremor episodes that consist of repeating velocity pulses (Fig. 3c). The spacing between the pulses changes from being as fast as 30 pulse s^{-1} to as slow as about 1 pulse s^{-1}. The pulse rate tends to change proportionally with the ice surface velocity during a large scale slip event. Additionally, at some stations the pulse rate is sufficiently low ($\lesssim 1$ Hz) that seismograms show individual *P* and *S* waves (Winberry et al., 2013).

A remarkable feature of the observed seismograms is seen in spectrograms as spectral peaks glide, or smoothly vary during the duration of large-scale sliding (Fig. 3a). The lowest frequency spectral peak occurs at the inverse of the pulse rate. This fundamental frequency $f_0(t)$ is accompanied by overtones that are present at integer multiples, i.e. $2f_0$, $3f_0$, and so on. We implement a basic feature tracking algorithm to calculate $f_0(t)$ from spectrograms of several tremor episodes and the result is shown in Fig. 4b.

Tremor episodes occur during all large-scale sliding events cataloged by Pratt et al. (2014) for which seismic data are available, and tremor episodes have never been observed when large-scale sliding is not occurring. Although some are more clearly visible than others, tremor episodes are observed at nearly every seismic station that has recently been deployed on the WIP. The tremor episodes are most clearly observed when more than three spectral peaks are present. Clearly observed tremor is most common at the stations BB09 and GS17, although stations BB02 and GS07 near BB09 also have multiple tremor bands. These three stations are located in regions of the WIP where more than 90 % of sliding occurs during large-scale slip events (Winberry et al., 2014c, their Fig. 3a), although not all stations located in such regions exhibit equally clear tremor. We primarily focus on data from BB09. When GPS data are not available for this station, we combine GPS data from BB02 with seismic data from BB09. These stations are located 6 km apart, and for an average rupture velocity on the order of 100–300 m s^{-1} (Walter et al., 2011, 2015), the resulting 20–60 s delay is small compared to the $\sim$ 1800 s duration of large-scale slip.

TCD
9, 5253–5289, 2015

Tremor episodes have peak seismic amplitudes on the order of 400–700 nm s^{-1}. An important terminology note is that we distinguish between high frequency particle velocity amplitudes v ("seismic amplitudes"), recorded using seismometers and ice surface velocities V_s recorded using GPS instruments. Quantifying the variation of seismic amplitudes with time is challenging because the data are noisy and broadband (Trigg, 2006, p. 99). We calculate the seismic particle velocity amplitude envelope using the following recursive algorithm. We first find all peaks in the time series, where a peak is any point that is larger than its two neighboring points. We then apply this same peak finder to the set of peaks, thereby eliminating smaller peaks. Recursion halts when the time between peaks in the remaining time series approaches ~ 10 s. The result seismic particle velocity amplitudes are shown for several tremor episodes in Fig. 4c.

The repeating velocity pulses each have duration on the order of 1/40 to 1/80 s. Pulse durations were mildly undersampled during the 2010–2011 field season when the sampling rate was 200 samples s^{-1}. During the 2011–2012 field season data was recorded at 500 samples s^{-1}; we refer to this latter data as the high rate data. To quantify the effects of undersampling, we examine 25 tremor episodes recorded at high rate at ten different seismometers. We observe no pulse duration less than 1/100 s. Extrapolating this finding to the data recorded at low rate suggests that we may interpret the pulse duration recorded at low-rate seismometers, even if it is only recorded over 3–6 data points. Undersampling may additionally result in amplitude reduction. We find that over the five tremor episodes that we examine from the second field season, the amplitude reduction that occurs by low pass filtering data below 100 Hz is 12.5 ± 0.5 %. We therefore correct the undersampled data from the first field season by scaling their amplitudes by a factor of 1.125.

We find that tremor episodes during double wait time events have higher seismic amplitudes than tremor episodes during single wait time events. To our knowledge, this association has not previously been noted. We quantify some implications of this finding in Sect. 7.

TCD
9, 5253–5289, 2015

3 Motion at the tremor-producing patch

We interpret each individual velocity pulse during a tremor episode as the far field expression of motion on a small fault patch. We refer to this patch as the tremor producing patch. Tremor episodes are interpreted as families or swarms of repeating earthquakes where the observed pulse rate is the earthquake recurrence rate.

At least two observations support this interpretation. First, small repeating earthquakes are expected to repeat with a faster recurrence rate at higher loading velocities, and this is observed in the data from the WIP. Second, at low pulse rate, Winberry et al. (2013) noted the presence of individually discernible events with clear P and S wave arrivals. This observation implies that tremor is composed of many rapidly repeating events rather than a resonance (Lipovsky and Dunham, 2015) or wave propagation effects (Bean et al., 2014).

Motion of the WIP is due to the longitudinal stresses that result from the push of upstream ice. This loading occurs within the ice column which causes most motion during large-scale slip events to occur in the ice rather than in the earth. We assume that the ice and the bed deform elastically, a valid approximation over the 15 min duration of a tremor episode (Fig. 2) (Goldberg et al., 2014). Throughout the earthquake cycle on the tremor patch, most motion occurs on the side of the patch that has the more compliant material (Fig. 2b, center panel).

Slip $\delta(\boldsymbol{x},t)$ at a point $\boldsymbol{x}$ on the ice–bed interface is defined as the difference in displacement between the upper and lower faces of the interface. Most of the bed experiences steady slip at nearly constant shear stress. This shear stress holds the bed in an elastically deformed state but causes no accelerations there. For this reason, the slip rate $V(\boldsymbol{x},t) = \partial\delta(\boldsymbol{x},t)/\partial t$ is equal to the surface velocity V_s

$$V = V_s. \tag{1}$$

When the tremor-producing patch is locked it experiences no slip and strain accumulates in time proportional to V_s (Fig. 2b, left panel).

TCD
9, 5253–5289, 2015

The tremor-producing patch experiences variations in the basal shear stress that give rise to stick-slip oscillations (Sect. 5). In this study we mostly focus on the spatially-averaged slip that occurs during a single earthquake,

$$D(t) = \int_{t}^{t+T} \int_{\substack{\text{tremor patch} \\ \text{surface}}} V(\boldsymbol{x}, t') \, \mathrm{d}A \, \mathrm{d}t', \tag{2}$$

where $T \sim 1/80$ s is the duration of slip.

The sliding velocity of the tremor-producing patch averaged over many slip cycles is approximately Df_0 for slip pulses that are evenly separated in time by f_0^{-1}. Over multiple earthquake cycles the sliding velocity must keep pace with the surface velocity of the ice V_s,

$$D = V_s / f_0. \tag{3}$$

Using observations of V_s and f_0, we infer values of $D \approx 15$–75 µm (Fig. 4d).

4 Wave propagation

We now describe the relationship between slip on the tremor-producing patch and the seismic particle velocity amplitudes recorded at on-ice seismometers. In our description, these amplitudes are influenced only by the accelerations on the tremor patch, tremor patch size, geometrical spreading, and potential bimaterial effects arising from the fault being located at the interface between ice and the bed material. Attenuation is thought to be unimportant at the frequencies of interest in the present study based on the following reasoning.

TCD
9, 5253–5289, 2015

The seismic quality factor Q is in the range 400–1000 over all of Antarctica (Peters et al., 2012). For wave propagation distances on the order of the ice thickness H, attenuation becomes important only at frequencies greater than a characteristic attenuation frequency

$$f_* \equiv Qc_\mathrm{i}/\pi H. \tag{4}$$

The shear wave speed of ice is denoted c_i. When $Q = 315$ this characteristic frequency is equal to 250 Hz, the highest Nyquist frequency in our data set. We therefore do not expect attenuation to be important for the frequencies that are resolved in our data set.

Far field seismic particle velocity due to fault motion in a uniform medium is given by (Aki and Richards, 2002, Eq. 4.96),

$$v(t) = \frac{\ddot{M}(t - H/c_\mathrm{i})}{4\pi\rho_\mathrm{i}c_\mathrm{i}^3 H}, \tag{5}$$

where the seismic moment is defined as

$$M(t) \equiv \pi G_\mathrm{i} R^2 D(t), \tag{6}$$

for a circular fault patch with radius R and ice shear modulus G_i. The overdot symbol denotes $\partial/\partial t$. We have made the simplifying assumption that the seismometer is located normal to the center of the fault plane. In this geometry, the seismometer does not record P waves because it is on a nodal plane, while S waves experience no amplitude reduction from radiation pattern effects. We assume that events are located at an epicentral distance of one ice thickness as was inferred by Winberry et al. (2013) on the basis of relative P–S wave arrivals.

The far field seismic velocity field predicted by Eq. (5) does not account for the contrast in material properties in the vicinity of the bed (Table 1). We consider two variations of Eq. (5) that account for material property heterogeneity.

TCD
9, 5253–5289, 2015

The first type of heterogeneity that we consider is that where the region surrounding the fault and the region surrounding the seismometer are both homogeneous but have different material properties. The far field seismic velocity is (Anandakrishnan and Bentley, 1993; Aki and Richards, 2002),

$$v(t) = \frac{\ddot{M}(t - H/c_\mathrm{i})}{2\pi\sqrt{z_\mathrm{i} z_\mathrm{b}}\, c_\mathrm{i}^2 H}, \tag{7}$$

where the shear wave impedances are denoted $z_k = \rho_k c_k$ (no summation) and z_i and z_b are the shear wave impedances of the ice and bed. The amplitudes predicted by Eq. (7) are valid for media with gradually varying material properties and may therefore be relevant to some aspects of ice sheet seismology (Wittlinger and Farra, 2012). The relationship Eq. (7), however, cannot account for the sharp changes in material properties that are expected to occur at the ice–bed interface.

The second type of heterogeneity that we consider is that where the fault patch is located at the ice–bed interface. A rich variety of wave behavior occurs when slip occurs along a fault that separates media with different elastic properties (Ben-Zion, 1990). We neglect head wave phases whose ray path partially travels along the bed. We take the short-time limit of Eq. (26) of Ben-Zion (1990) and find that the far field particle velocity amplitudes are sensitive to the material properties on both sides of the fault through the impedance parameter Z,

$$Z = \frac{z_\mathrm{b}}{z_\mathrm{i} + z_\mathrm{b}}. \tag{8}$$

Seismic moment Eq. (6) is not well defined for slip on a bimaterial interface (Ampuero and Dahlen, 2005), in which case a more useful quantity is seismic potency,

$$P(t) \equiv \pi R^2 D(t). \tag{9}$$

TCD
9, 5253–5289, 2015

Far-field seismic particle velocity amplitudes are given by

$$v(t) = Z\frac{\ddot{P}(t - H/c_i)}{\pi c_i H}. \quad (10)$$

We have invoked a factor of two higher amplitudes to account for amplification at the free surface.

We find a scaling relationship for the far field particle velocity Eq. (10) by replacing time derivatives with the event duration T:

$$v \sim Z\frac{D}{c_i H}\left(\frac{R}{T}\right)^2. \quad (11)$$

The factor of R/T has the interpretation of a rupture velocity, and it is interesting to note that at constant slip D and for constant material properties, seismic amplitudes depend only on this rupture velocity.

5 Forces acting on the fault patch

5.1 The elastic response

We now examine the forces acting on the tremor-producing patch. Slip on the patch D is related to the static stress drop $\Delta\tau$ through the relationship

$$\Delta\tau = kD \equiv \frac{G_*}{R}D. \quad (12)$$

The modulus G_* denotes the effective patch shear modulus of the bimaterial interface. The patch stiffness k depends on the elastic constants on both sides of the sliding interface and has units of stress per length. For the case where the material properties on both sides of the fault are identical, $G_* = (16G/7\pi)$ when the Poisson ratio $\nu = 1/4$.

TCD
9, 5253–5289, 2015

We calculate the patch stiffness for a circular fault on a bimaterial interface. This calculation is carried out by taking derivatives of the strain energy function of Willis (1971) as described by Aki and Richards (2002) in their Eq. (2.31). In the limiting case where one material is much more rigid than the other, G_* becomes independent of the elastic properties of the more rigid material and

$$G_* \approx 2G_{\text{compliant}} \text{ for } \nu = 1/4. \tag{13}$$

The shear stress τ experienced by the small fault patch is

$$\frac{\mathrm{d}\tau}{\mathrm{d}t} = -k(V - V_\mathrm{s}) - \eta\frac{\mathrm{d}V}{\mathrm{d}t}, \tag{14}$$

where V is the sliding velocity on the patch surface, t is time, and the radiation damping parameter is (Geubelle and Breitenfeld, 1997),

$$\eta \equiv \left(\frac{1}{z_\mathrm{i}} + \frac{1}{z_\mathrm{b}}\right)^{-1}. \tag{15}$$

The right hand side of Eq. (14) represents the contribution to the shear stress rate due to elasticity. The first term is the static elastic stressing rate. Static elastic strains accumulate in the region surrounding the fault during the period between slip pulses. The static elastic stress term describes the contribution to the stressing rate from this loading. The second term is an approximate inertial stressing rate. In an instantaneous amount of time after slip initiates on the fault patch, shear waves emanate away from the patch and have a damping effect. The radiation damping term accounts for the stress change carried by these waves.

The duration of slip arises from a balance between these two terms and is given by

$$T \equiv \frac{\eta}{k} \sim \frac{R\eta}{G_*} \sim 1/f_\mathrm{c}, \tag{16}$$

TCD
9, 5253–5289, 2015

where the corner frequency is denoted f_c. Equation (16) is a scaling law for the earthquake duration and not an equality (Brune, 1970; Madariaga, 1976; Kaneko and Shearer, 2014). Actual earthquake durations vary for many reasons including variable rupture velocity and whether a rupture is bilateral or unilateral. We expect these additional features to introduce factors of order unity into Eq. (16). For the purposes of this study, we consider Eq. (16) to be adequate.

5.2 Friction

Elastic forces are balanced by friction. Frictional stresses change in time according to

$$\frac{\mathrm{d}\tau}{\mathrm{d}t} = \frac{a\bar{\sigma}}{V}\frac{\mathrm{d}V}{\mathrm{d}t} - \frac{V}{L}\left[\tau - f_{\mathrm{ss}}(V)\bar{\sigma}\right], \tag{17}$$

where $\bar{\sigma} = \sigma - p$ is the effective pressure due to normal stress σ and pore pressure p. The steady state coefficient of friction $f_{\mathrm{ss}}(V)$ is given by

$$f_{\mathrm{ss}}(V) = f_0 - (b-a)\log(V/V_0). \tag{18}$$

The parameters f_0, a, b, and V_0 are the nominal coefficient of friction, the direct effect parameter, the healing parameter, and the reference velocity. The first term on the right hand side of Eq. (17) represents the laboratory-observed instantaneous increase of frictional resistance to sliding with an increase in sliding velocity. The magnitude of this so-called direct effect is characterized by the parameter a. The second term on the right hand side of Eq. (17) represents the evolution of frictional resistance to a steady state value $f_{\mathrm{ss}}(V)$ that depends on the sliding velocity. This evolution occurs over the state evolution distance L. The change in steady frictional resistance to sliding Eq. (18) at two different sliding velocities is proportional to $(b-a)$ and to the logarithm of the ratio of the velocities.

The appropriateness in glaciology of a friction law of this type has been demonstrated by numerous studies (Thomason and Iverson, 2008; Rathbun et al., 2008; Iverson,

TCD
9, 5253–5289, 2015

2010; Zoet et al., 2013). These studies examined the frictional properties of till-on-clast sliding (Thomason and Iverson, 2008), till-on-till sliding (Rathbun et al., 2008), and ice-on-rock sliding (Zoet et al., 2013). Each conducted velocity-step and slide-hold-slide experiments, Thomason and Iverson (2008) on a ring-shear device and Rathbun et al. (2008) and Zoet et al. (2013) in a biaxial shear apparatus. A description such as Eq. (17) may be thought of as a refinement to the generally accepted frictional-plastic rheological description of till (Tulaczyk et al., 2000) and as generalization of a frictional model consisting only of static and dynamic coefficients of friction (e.g., Sergienko et al., 2009).

5.3 Stability of steady sliding

The system of Eqs. (14), (17), and (18) is amenable to traditional linear stability analysis. One prediction of such an analysis is the condition under which the stick-slip instability occurs. This type of analysis was carried out by Dmitrieva et al. (2013) for perturbations about steady sliding at rate V_s. Dmitrieva et al. (2013) found that the transition between steady sliding and stick-slip motion occurs when (their supplemental Eq. 8),

$$\frac{(b-a)\bar{\sigma}}{L} \geq k + \frac{\eta V_s}{L}. \tag{19}$$

Equality in Eq. (19) is achieved at neutral stability. Dependence on the patch size R enters Eq. (19) through the patch stiffness k. The left hand side of Eq. (19) represents the variation in frictional strength per slip increment $\mathrm{d}\tau_{str}/\mathrm{d}D$. The right hand side of Eq. (19) represents the variation in elastic stress per slip increment $\mathrm{d}\tau_{el}/\mathrm{d}D$.

The stability condition Eq. (19) has two dominant balances that result from balancing each of the elastic components with the strength term. The static stability limit occurs when $(b-a)\bar{\sigma}$ is balanced by kL. In this limit, the sliding is stabilized by the static elastic stiffness of the near-fault material. The inertial stability limit occurs when $(b-a)\bar{\sigma}$ is

TCD
9, 5253–5289, 2015

balanced by ηV. In this limit, sliding is stabilized by the damping effect of waves that are radiated during periods of higher sliding velocity.

5.4 Simulations of tremor events

We carry out simulations of a spring slider system that obeys the governing Eqs. (14), (17), and (18). We use observed surface velocity data recorded on the ice to load the fault in our simulations, i.e., the loading velocity is set equal to the observed surface velocity as measured by a GPS station deployed on the Whillans Ice Stream at station BB09. The GPS data are interpolated using a cubic spline. The system of equations is solved in MATLAB using the Runge–Kutta solver *ode45*.

In the next section we describe parameterizations of subglacial conditions that allow us to approximately match the observed seismograms. With careful choice of parameters, we are able to match the primary features of the observed spectrograms. An example is shown in Fig. 3. We match the observed variation of $f_0(t)$ during most of the period of elevated sliding, as well as seismic amplitudes and corner frequencies recorded at the seismometer BB09. We show a time slice of the spectrogram at $t = 400$ s, where $t = 0$ corresponds to the time of maximum sliding velocity, in Fig. 3c.

6 Inferences of subglacial conditions

We now place constraints on the bed shear modulus G_b, the effective pressure $\bar{\sigma}$, the patch size R, and the state evolution distance L. We hold all other parameters fixed except where explicitly mentioned (see Table 1). We first discuss the choice of frictional parameters.

6.1 Frictional parameters

The frictional parameters are chosen to have the values $a = 0.010$ and $b = 0.015$ which are typical of glacial materials (Thomason and Iverson, 2008; Rathbun et al., 2008;

TCD
9, 5253–5289, 2015

Iverson, 2010; Zoet et al., 2013). One effect of varying these frictional parameters is to alter a lower bound on effective pressure. This lower bound is given by the inertial stability limit of Eq. (19) and results in a direct trade-off between the frictional parameter $b - a$ and effective pressure $\bar{\sigma}$,

$$\bar{\sigma} = \frac{\eta V_s}{b - a}. \tag{20}$$

Using a $b-a$ values in the range $10^{-3}-10^{-1}$ and the maximum observed sliding velocity gives a lower bound in the range $\bar{\sigma} \gtrsim 1$–100 kPa. For our preferred value $b - a = 0.01$, $\bar{\sigma} \gtrsim 10$ kPa. As we will discuss in Sect. 6.3, effective pressures in the upper part of this range require small patches and are not consistent with observed corner frequencies ~ 100 Hz.

6.2 Constraints on the bed shear modulus from seismic amplitudes

The shear modulus of the bed is directly constrained by combining the scaling relationships for the particle velocity amplitude Eq. (11) and event duration Eq. (16). The resulting scaling relation is

$$v \sim Z(G_b)\frac{D}{c_i H}\left[\frac{k(G_b)}{\eta(G_b)}\right]^2. \tag{21}$$

The only quantity that is not held fixed in Eq. (21) is the shear modulus of the bed G_b.

We solve Eq. (21) as a function of time several tremor episodes. The result is plotted in Fig. 5. The bed shear modulus over all times and events has mean 13 MPa with standard deviation 2.3 MPa. For till density in the range 1700–2200 kg m^{-3} this suggests till shear wave speeds ~ 75–100 m s^{-1}. This value is in rough agreement with previous studies, as we will describe in Sect. 8.

TCD
9, 5253–5289, 2015

6.3 Constraints on patch size and effective pressure from fault stability and stress analysis

We now constrain conditions to lie along a one-dimensional subset of patch size-effective pressure space ($R - \bar{\sigma}$ space) that is consistent with observed slip D. Having constrained the bed shear modulus in Sect. 6.2, we now hold this quantity fixed. This subset is then further refined by requiring that simulated tremor episodes also match observed corner frequencies.

We use three constraints: (1) effective pressure cannot exceed the overburden pressure, (2) fault conditions must be unstable in order to support the existence of stick slip motion Eq. (19), and (3) slip per event D must match that inferred from V_s/f_0 Eq. (3). These three conditions are plotted in $R, \bar{\sigma}$ space in Fig. 6. The three parameter space constraints correspond to (1) a horizontal line indicating the overburden pressure, (2) a curve indicating the stability condition, and (3) a heavy line indicating the $\bar{\sigma}, R$ combinations that produce the observed slip D. The points along this line of observed slip are found by solving the minimization problem $\|D(\bar{\sigma}, R) - D_{\text{obs}}\|$ where the slip per event at a given effective pressure and patch size $D(\bar{\sigma}, R)$ is calculated using numerical simulations.

Different $\bar{\sigma}, R$ combinations that match observed displacements are distinguished by having different corner frequencies, f_c. This is shown in the inset of Fig. 6. We recall that because we hold the bed shear modulus and slip fixed, Eq. (21) shows that seismic amplitudes do not vary for any points along the line of constant slip. Taking the corner frequency to lie in the range 50–100 Hz constrains patch size to be in the range 1.2–2.4 m. The corresponding estimates of effective pressure are between 15 kPa for larger patch sizes and 30 kPa for smaller patch sizes.

TCD
9, 5253–5289, 2015

6.4 State evolution distance

We infer a state evolution distance no greater than $\sim 1\,\mu m$. This claim is verified as follows. The stability condition Eq. (19) may be written, using the stress drop relationship Eq. (12) and the duration scaling Eq. (16) as

$$D \gtrsim V_s T + L, \tag{22}$$

where we have assumed that the stress drop scales with $(b - a)\bar{\sigma}$. Instability therefore occurs when fault slip D is greater than the critical slip distance L plus any additional slip deficit $V_s T$ that has accumulated during the slip event. The relationship Eq. (22) predicts $L \lesssim 5\,\mu m$ for the extreme values of the parameters observed on the WIP.

A tighter constraint on L comes from the linear stability analysis of Dmitrieva et al. (2013). We rewrite their expression for the recurrence frequency (their supplemental Eq. 10) as

$$f_0 = \frac{1}{2\pi}\frac{V_s}{L}\sqrt{\frac{kL}{a\bar{\sigma} + \eta V_s}}. \tag{23}$$

Solving for L, we find

$$L = \frac{V_s^2 k}{(2\pi f_0)^2 (a\bar{\sigma} + \eta V_s)} \approx 1\,\mu m, \tag{24}$$

where we have assumed tremor frequencies $\sim 20\,Hz$ and used our previously stated parameter estimates. Micron-scale L values are on the small end of values typically inferred for geological and engineered materials (Dieterich, 2007). The critical slip distance is generally thought to be related to a material's grain size. In the case of sliding against glacial till, inferred μm L values may result from the high clay content, and therefore μm-scale grain size, of WIS till (Tulaczyk et al., 1998).

TCD
9, 5253–5289, 2015

7 Variation of seismic amplitude at constant slip

Tremor episodes during the two large-scale sliding events on 14 January 2011 illustrate an interesting phenomenon. The morning event was a double wait time event and the afternoon event was a single wait time event. Although they have similar slip they have seismic amplitudes that differ by 30 % (Fig. 4). The contrast in seismic amplitudes for these two events is particularly notable during the time range $t = 200$–400 s. This difference is notable because from Eq. (11) we expect that two repeating earthquakes with the same slip and with all other parameters equal should have the same seismic amplitude.

We consider two mechanisms for the observed seismic amplitude variation at constant slip D. First, from the analysis in Sect. 6.2, we expect that the difference in amplitudes at constant slip D may only arise from changes in the bed shear modulus. Indeed, Fig. 5 shows that the inferred shear modulus during this period is 14 MPa for the morning event and 18 MPa for the afternoon event, a ~ 30 % change. The second explanation is that the variation is due to unmodeled effects involving partitioning between seismic and aseismic slip.

7.1 Explanation 1: actual stiffness change

The first mechanism we discuss is that the apparent variation in bed stiffness is real and involves the granular mechanics of till. Granular material such as glacial till have elastic moduli that depend on effective pressure (Mavko et al., 2009, ch. 5.2). When a pack of grains is subjected to an increase in effective pressure the total area of contact between the grains increases. The length scale associated with this contact area governs the strain magnitude in the grain pack and therefore sets the bulk stiffness of the grain pack. Digby (1981) describes the resulting change in elastic modulus under the assumptions of spherical particle geometry and small strains. We estimate the change in shear modulus as a function of confining pressure as described by Mavko et al. (2009). We assume coordination number $C = 9$, grain shear modulus 40 GPa, and grain Poisson

TCD
9, 5253–5289, 2015

ratio 0.15. We choose a value for the fractional initial contact area, 0.1 %, that is taken to represent a loosely packed particle arrangement.

We calculate that a 30 % increase in the bulk shear modulus requires increasing effective pressure by a factor of 2.5 (e.g., from 10 to 25 kPa). If we assume a higher initial contact area of 1 %, then a 30 % increase in the bulk shear modulus requires increasing effective pressure by a factor of 25 (e.g., from 10 to 250 kPa).

One limitation of this explanation is that the bed material may not be well represented as a pack of elastic spheres. WAIS subglacial till consists of an unsorted mixture of ~ 30 % sand-sized particles and more than 30 % clay-sized particles by weight (Tulaczyk et al., 1998). The sand fraction is well approximated spherical particles; the clay fraction, because of its two-dimensional sheet structure, is not. It is not clear a priori whether the bulk stiffness of the bed material is governed by one of these phases or both. If the bulk stiffness is governed by clay phases, the basic scaling of the elastic moduli predicted by Digby (1981) may be inapplicable. Despite this shortcoming, it is not unreasonable to assume that till exhibits pressure dependence of its elastic moduli, and for this reason we do not rule out this potential explanation.

7.2 Explanation 2: aseismic slip

Another explanation is that seismic amplitudes are lower for single wait time events because more of their slip occurs aseismically. Several studies provide an observational basis for the occurrence of combined seismic and aseismic motion along isolated fault patches at ice stream beds (Anandakrishnan et al., 2001; Smith et al., 2015). This phenomenon is not necessarily captured by our idealized fault model as it requires the calculation of the spatial variation of stress and slip along the finite extent of the fault patch. Simulations that do calculate this variation, however, show that more aseismic sliding is expected to occur as a fault approaches the stability limit (Chen and Lapusta, 2009). Although our description of stress and slip on the fault does not capture this behavior, several other aspects of our description remain approximately valid for a finite fault.

TCD
9, 5253–5289, 2015

When some fault motion is aseismic, the total slip during the seismic cycle consists of an aseismic part and a seismic part, $D = D_A + D_S$. The kinematic condition Eq. (3) must hold for the total slip, so that $D = V_s/f_0$. Seismic amplitudes, however, are sensitive only to seismic slip. Aseismic slip therefore explains lower seismic amplitudes for single wait time events if single wait time events experience some aseismic slip.

Aseismic slip is favored for smaller magnitude events (Chen and Lapusta, 2009, their Fig. 8) as fault conditions approach stability. This could happen for a variety of reasons, including decreasing either the fault radius or effective pressure. Implications of such changes for the long term deceleration of the WIP are discussed in Sect. 8. A complete description of the potential conditions which lead to aseismic slip in the context of the subglacial environment is not currently available in the literature and further investigation in this area is certainly warranted.

8 Discussion

We have quantified the dynamics of a small fault patch at the bed of an ice stream using a spring-slider model. Motions on the fault excite seismic waves and by comparing synthetic seismograms with those that are observed we have constrained several fault zone parameters. We are able to match many of the remarkable features of the tremor episodes recorded on the Whillans Ice Plain (Fig. 3), including the variation of tremor spectral peaks with sliding velocity, seismic amplitudes, and corner frequencies.

Our simulations have constant fault zone properties throughout the tremor episode. As a result of this, our simulations do not always match the observed seismic amplitudes and recurrence frequencies during an entire tremor episode (Fig. 4). This self-imposed limitation may seem contradictory because we have just argued that the fault zone properties appear to change during a tremor episode (Fig. 5). We accept this limitation because of the possibility that 2-D or 3-D effects are involved in the observed temporal evolution during a single event.

TCD
9, 5253–5289, 2015

Tremor episodes in glaciers may also be related to the motions of fluids contained within conduits (Métaxian et al., 2003; Stuart et al., 2005; Winberry et al., 2009; Gimbert et al., 2014; Lipovsky and Dunham, 2015; Bartholomaus et al., 2015). Several lines of evidence suggest that the WIP tremor episodes are not related to such a source process. The foremost reason is that on certain seismometers, tremor episodes clearly show individual slip events with clear *P* and *S* wave arrivals (Winberry et al., 2013). Additionally, there is a strong correlation between observed ice surface velocities and the tremor frequency and this correlation has a clear interpretation in terms of repeating earthquakes. The relationship between surface velocities and hydraulic fracture resonance, in contrast, is not as clear. Finally, simple models of hydraulic fracture resonance (Lipovsky and Dunham, 2015) and turbulent channel flow (Gimbert et al., 2014) predict spectral signatures that are not consistent with the evenly spaced spectral peaks observed on the WIP, although complex geometrical effects may invalidate the simplifying assumptions of such models. These distinguishing criteria may be useful in analyzing several recently described data sets (Heeszel et al., 2014; Helmstetter et al., 2015a, b; Hammer et al., 2015).

Having identified a bed shear wave speed of 75–100 $\mathrm{m\,s^{-1}}$ in Sect. 6.2, we rule out the possibility that the tremor producing patch is a bedrock outcrop. We consider this inferred shear wave speed to be consistent with the presence of subglacial till (Blankenship et al., 1986). Further evidence that the fault interface consists at least partly of till is also given by the relatively small estimated state evolution distance $L \sim 1\,\mu\mathrm{m}$. We interpret this distance to be indicative of sliding against a material with µm-scale grain size, and glacial till is the most plausible such material (Tulaczyk et al., 1998).

The WIP has long been recognized to have heterogeneous basal shear resistance (Alley, 1993). Direct borehole access to the bed has measured effective pressure in the range of −30 to 200 kPa (Kamb, 2001). Numerous ice flow model-based inversions of geodetic data have found localized regions of high basal shear stress in the vicinity of the seismometers that record the WIP tremor episodes (Joughin et al., 2004; Winberry

TCD
9, 5253–5289, 2015

et al., 2014c; Sergienko et al., 2014). In particular, recent inversions with precise digital elevation data show that shear resistance in localized (sub-km) patches may be as high as 10–100 kPa. These patches exist within extensive regions that have zero shear resistance within the resolution of the inversion (O. Sergienko, personal communication, 2015). Our estimated ∼ 10 kPa effective pressure within the tremor fault zone is therefore in reasonable agreement with both borehole and geodetic stress estimates.

Our 100 Pa stress drop estimate is somewhat low but not unusual for glacier sliding earthquakes. On the Hans Glacier, Svalbard, Górski (2014) find fault radii of 28–74 m associated with stress drops 86 Pa–1.2 kPa, respectively. On upstream sites on the Kamb and Whillans Ice Streams, Anandakrishnan and Alley (1994) find fault radii of 5–10 m associated with stress drops of 10–100 kPa, respectively. On the David Glacier, East Antarctica, Danesi et al. (2007) find fault radii 65–110 m associated with stress drops 100–600 kPa, respectively. The data of Górski (2014) show spectral troughs that are likely due to free surface reflections, and so their estimates of fault size should be interpreted as lower bounds (Langston, 1978). The range of stress drops given by Danesi et al. (2007) occurs because they do not account for bimaterial effects and instead consider end-member elastic moduli scenarios.

Tremor events may provide insight into the mechanism of long term deceleration at the WIP. Double wait time events are becoming more common during WIP stagnation (Winberry et al., 2014c). The particular conditions that give rise to higher seismic amplitudes during double wait time events (Sect. 7) may therefore be indicative of prevailing near-future conditions of the WIP. We now discuss the markedly different predictions of each of the two mechanisms we have identified to account for this behavior.

The two mechanisms identified to account for anomalous seismic amplitudes make different predictions about fault zone stability: a stiffening bed implies a shift towards more stable conditions, but increased seismic slip implies a shift towards less stable conditions. Independent observations seem to favor the hypothesis that during ice stream stagnation the bed becomes more unstable to sliding. The stagnant Kamb Ice Stream, for example, has a seismicity rate that is approximately 1000 times higher

TCD
9, 5253–5289, 2015

than on the fast flowing, upstream part of the Whillans Ice Stream (Anandakrishnan and Bentley, 1993; Anandakrishnan and Alley, 1994, 1997). One interpretation of this observation is that as an ice stream decelerates, subglacial conditions become more unstable in the sense defined by Eq. (19). This scenario is consistent with increasing effective pressure (at constant slip, D, see Fig. 6) and is therefore consistent with a water piracy-type mechanism for ice stream stagnation (Alley et al., 1994; Anandakrishnan and Alley, 1997).

We have conducted dynamic simulations of stick slip motion at the bed of the Whillans Ice Plain (WIP). By comparing the simulations to data, we are able to independently infer the presence of an elastically compliant, fine-grained till layer and high pore pressures. Furthermore, seismic amplitude variations between tremor episodes may be related to long term changes occurring at the bed.

Data availability

The seismic data used in this study were downloaded from IRIS (http://www.fdsn.org/networks/detail/2C_2010). The geodetic data were obtained from Winberry et al. (2014a, b).

Acknowledgements. This manuscript benefitted from discussions with J. Paul Winberry, Martin Pratt, Slawek Tulaczyk, Grace Barcheck, Susan Schwartz, Cooper Elsworth, Greg Beroza, Hilmar Gudmundson, and Yehuda Ben-Zion.

References

Aki, K. and Richards, P. G.: Quantitative Seismology, University Science Books, Sausalito, California, USA, 2002. 5261, 5262, 5264

Alley, R. B.: In search of ice-stream sticky spots, in: vol. 1, West Antarctic Ice Sheet (WAIS) Science Workshop, Arlington, Virginia, USA, p. 36, 1993. 5274

TCD
9, 5253–5289, 2015

Alley, R. B., Anandakrishnan, S., Bentley, C., and Lord, N.: A water-piracy hypothesis for the stagnation of Ice Stream C, Antarctica, Ann. Glaciol., 20, 187–194, 1994. 5276
Ampuero, J.-P. and Dahlen, F.: Ambiguity of the moment tensor, Bull. Seis. Soc. Amer., 95, 390–400, 2005. 5262
Anandakrishnan, S. and Alley, R.: Ice Stream C, Antarctica, sticky spots detected by microearthquake monitoring, Ann. Glaciol., 20, 183–186, 1994. 5275, 5276
Anandakrishnan, S. and Alley, R. B.: Stagnation of Ice Stream C, West Antarctica by water piracy, Geophys. Res. Lett., 24, 265–268, 1997. 5276
Anandakrishnan, S. and Bentley, C.: Micro-earthquakes beneath Ice Streams B and C, West Antarctica: observations and implications, J. Glaciol., 39, 455–462, 1993. 5262, 5276
Anandakrishnan, S., Alley, R., Jacobel, R., and Conway, H.: The flow regime of Ice Stream C and hypotheses concerning its recent stagnation, The West Antarctic Ice Sheet: Behavior and Environment, AGU Antarct. Res. Ser., 77, 283–296, 2001. 5272
Bartholomaus, T. C., Amundson, J. M., Walter, J. I., O'Neel, S., West, M. E., and Larsen, C. F.: Subglacial discharge at tidewater glaciers revealed by seismic tremor, Geophys. Res. Lett.,doi:10.1002/2015GL064590, in press, 2015. 5274
Bean, C. J., De Barros, L., Lokmer, I., Métaxian, J.-P., O'Brien, G., and Murphy, S.: Long-period seismicity in the shallow volcanic edifice formed from slow-rupture earthquakes, Nat. Geosci., 7, 71–75, 2014. 5259
Beem, L., Tulaczyk, S., King, M., Bougamont, M., Fricker, H., and Christoffersen, P.: Variable deceleration of Whillans Ice Stream, West Antarctica, J. Geophys. Res., 119, 212–224, doi:10.1002/2013JF002958, 2014. 5254
Ben-Zion, Y.: The response of two half spaces to point dislocations at the material interface, Geophys. J. Int., 101, 507–528, 1990. 5262
Bindschadler, R. A., King, M. A., Alley, R. B., Anandakrishnan, S., and Padman, L.: Tidally controlled stick-slip discharge of a West Antarctic ice stream, Science, 301, 1087–1089, doi:10.1126/science.1087231, 2003. 5255, 5256
Blankenship, D. D., Bentley, C. R., Rooney, S., and Alley, R. B.: Seismic measurements reveal a saturated porous layer beneath an active Antarctic ice stream, Nature, 322, 54–57, doi:10.1038/322054a0, 1986. 5274
Bougamont, M., Price, S., Christoffersen, P., and Payne, A.: Dynamic patterns of ice stream flow in a 3-D higher-order ice sheet model with plastic bed and simplified hydrology, J. Geophys. Res., 116, F04018, doi:10.1029/2011JF002025, 2011. 5255

TCD
9, 5253–5289, 2015

Brune, J.: Tectonic Stress and the Spectra of Seismic Shear Waves from Earthquakes, J. Geophys. Res., 75, 4997–5009, doi:10.1029/JB075i026p04997, 1970. 5265
Chen, T. and Lapusta, N.: Scaling of small repeating earthquakes explained by interaction of seismic and aseismic slip in a rate and state fault model, J. Geophys. Res., 114, B01311, doi:10.1029/2008JB005749, 2009. 5272, 5273
Danesi, S., Bannister, S., and Morelli, A.: Repeating earthquakes from rupture of an asperity under an Antarctic outlet glacier, Earth Planet. Sc. Lett., 253, 151–158, doi:10.1016/j.epsl.2006.10.023, 2007. 5275
Dieterich, J.: Applications of rate-and state-dependent friction to models of fault slip and earthquake occurrence, Treat. Geophys., 4, 107–129, 2007. 5270
Digby, P.: The effective elastic moduli of porous granular rocks, J. Appl. Mech., 48, 803–808, 1981. 5271, 5272
Dmitrieva, K., Hotovec-Ellis, A. J., Prejean, S., and Dunham, E. M.: Frictional-faulting model for harmonic tremor before Redoubt Volcano eruptions, Nat. Geosci., 6, 652–656, doi:10.1038/ngeo1879, 2013. 5266, 5270
Geubelle, P. and Breitenfeld, M.: Numerical analysis of dynamic debonding under anti-plane shear loading, Int. J. Frac., 85, 265–282, doi:10.1023/A:1007498300031, 1997. 5264
Gimbert, F., Tsai, V. C., and Lamb, M. P.: A physical model for seismic noise generation by turbulent flow in rivers, J. Geophys. Res., 119, 2209–2238, doi:10.1002/2014JF003201, 2014. 5274
Goldberg, D., Schoof, C., and Sergienko, O.: Stick-slip motion of an Antarctic Ice Stream: the effects of viscoelasticity, J. Geophy. Res., 119, 1564–1580, doi:10.1002/2014JF003132, 2014. 5259
Górski, M.: Seismic Events in Glaciers, Springer, Heidelberg, 2014. 5275
Hammer, C., Ohrnberger, M., and Schlindwein, V.: Pattern of cryospheric seismic events observed at Ekström ice shelf, Antarctica, Geophys. Res. Lett., doi:10.1002/2015GL064029, in press, 2015. 5274
Haran, T., Bohlander, J., Scambos, T., Painter, T., and Fahnestock, M.: MODIS Mosaic of Antarctica 2008–2009 (MOA2009) Image Map, National Snow and Ice Data Center, Boulder, CO, USA, 10, N5KP8037, 2014. 5284
Heeszel, D. S., Walter, F., and Kilb, D. L.: Humming glaciers, Geology, 42, 1099–1102, 2014. 5274

TCD
9, 5253–5289, 2015

Helmstetter, A., Moreau, L., Nicolas, B., Comon, P., and Gay, M.: Intermediate-depth icequakes and harmonic tremor in an Alpine glacier (Glacier d'Argentière, France): evidence for hydraulic fracturing?, J. Geophys. Res., 120, 402–416, 2015a. 5274

Helmstetter, A., Nicolas, B., Comon, P., and Gay, M.: Basal icequakes recorded beneath an Alpine glacier (Glacier d'Argentière, Mont Blanc, France): evidence for stick-slip motion?, J. Geophys. Res., 120, 379–401, 2015b. 5274

Iverson, N. R.: Shear resistance and continuity of subglacial till: hydrology rules, J. Glaciol., 56, 1104–1114, doi:10.3189/002214311796406220, 2010. 5265, 5268

Joughin, I. and Alley, R. B.: Stability of the West Antarctic ice sheet in a warming world, Nat. Geosci., 4, 506–513, 2011. 5254

Joughin, I., MacAyeal, D. R., and Tulaczyk, S.: Basal shear stress of the Ross ice streams from control method inversions, J. Geophys. Res., 109, B09405, doi:10.1029/2003JB002960, 2004. 5274

Kamb, B.: Basal zone of the West Antarctic ice streams and its role in lubrication of their rapid motion, in: The West Antarctic Ice Sheet: Behavior and Environment, American Geophysical Union, Washington, D.C., 157–199, 2001. 5274

Kaneko, Y. and Shearer, P.: Seismic source spectra and estimated stress drop derived from cohesive-zone models of circular subshear rupture, Geophys. J. Int., doi:10.1002/2014JB011642, in press, 2014. 5265

Kyrke-Smith, T., Katz, R., and Fowler, A.: Subglacial hydrology and the formation of ice streams, P. Roy. Soc. Lond., 470, 20130494, doi:10.1098/rspa.2013.0494, 2014. 5255

Kyrke-Smith, T., Katz, R., and Fowler, A.: Subglacial hydrology as a control on emergence, scale and spacing of ice streams, J. Geophys. Res., doi:10.1002/2015JF003505, in press, 2015. 5255

Langston, C. A.: Moments, corner frequencies, and the free surface, J. Geophys. Res., 83, 3422–3426, 1978. 5275

Lipovsky, B. P. and Dunham, E. M.: Vibrational modes of hydraulic fractures: Inference of fracture geometry from resonant frequencies and attenuation, J. Geophys. Res., 120, 1080–1107, doi:10.1002/2014JB011286, 2015. 5259, 5274

MacAyeal, D., Okal, E., Aster, R., and Bassis, J.: Seismic and hydroacoustic tremor generated by colliding icebergs, J. Geophys. Res., 113, F03011, doi:10.1029/2008JF001005, 2008. 5255

TCD
9, 5253–5289, 2015

Madariaga, R.: Dynamics of an expanding circular fault, B. Seismol. Soc. Am., 66, 639–666, 1976. 5265
Mavko, G., Mukerji, T., and Dvorkin, J.: The Rock Physics Handbook: Tools for Seismic Analysis of Porous Media, Cambridge University Press, 2009. 5271
Métaxian, J.-P., Araujo, S., Mora, M., and Lesage, P.: Seismicity related to the glacier of Cotopaxi Volcano, Ecuador, Geophys. Res. Lett., 30, 1483, doi:10.1029/2002GL016773, 2003. 5274
Peters, L., Anandakrishnan, S., Alley, R., and Voigt, D.: Seismic attenuation in glacial ice: A proxy for englacial temperature, J. Geophys. Res., 117, F02008, doi:10.1029/2011JF002201, 2012. 5261
Powell, T. and Neuberg, J.: Time dependent features in tremor spectra, J. Volcanol. Geoth. Res., 128, 177–185, 2003. 5255
Pratt, M. J., Winberry, J. P., Wiens, D. A., Anandakrishnan, S., and Alley, R. B.: Seismic and geodetic evidence for grounding-line control of Whillans Ice Stream stick-slip events, J. Geophys. Res., 119, 333–348, doi:10.1002/2013JF002842, 2014. 5255, 5257
Rathbun, A. P., Marone, C., Alley, R. B., and Anandakrishnan, S.: Laboratory study of the frictional rheology of sheared till, J. Geophys. Res., 113, F02010, doi:10.1029/2007JF000815, 2008. 5265, 5266, 5267
Rignot, E., Mouginot, J., and Scheuchl, B.: Ice flow of the Antarctic ice sheet, Science, 333, 1427–1430, doi:10.1126/science.1208336, 2011. 5254
Robel, A. A., DeGiuli, E., Schoof, C., and Tziperman, E.: Dynamics of ice stream temporal variability: Modes, scales, and hysteresis, J. Geophys. Res., 118, 925–936, doi:10.1002/jgrf.20072, 2013. 5255
Scambos, T., Haran, T., Fahnestock, M., Painter, T., and Bohlander, J.: MODIS-based Mosaic of Antarctica (MOA) data sets: Continent-wide surface morphology and snow grain size, Remote Sens. Environ., 111, 242–257, 2007. 5284
Sergienko, O. V., MacAyeal, D. R., and Bindschadler, R. A.: Stick–slip behavior of ice streams: modeling investigations, Ann. Glaciol., 50, 87–94, 2009. 5266
Sergienko, O. V., Creyts, T., and Hindmarsh, R.: Similarity of organized patterns in driving and basal stresses of Antarctic and Greenland ice sheets beneath extensive areas of basal sliding, Geophys. Res. Lett., 41, 3925–3932, doi:10.1002/2014GL059976, 2014. 5275

TCD
9, 5253–5289, 2015

Smith, E., Smith, A., White, R., Brisbourne, A., and Pritchard, H.: Mapping the Ice-Bed Interface Characteristics of Rutford Ice Stream, West Antarctica, Using Microseismicity, J. Geophys. Res., accepted, 2015. 5272

Stuart, G., Murray, T., Brisbourne, A., Styles, P., and Toon, S.: Seismic emissions from a surging glacier: Bakaninbreen, Svalbard, Ann. Glaciol., 42, 151–157, doi:10.3189/172756405781812538, 2005. 5274

Thomason, J. F. and Iverson, N. R.: A laboratory study of particle ploughing and pore-pressure feedback: a velocity-weakening mechanism for soft glacier beds, J. Glaciol., 54, 169–181, doi:10.3189/002214308784409008, 2008. 5265, 5266, 5267

Trigg, G.: Mathematical Tools for Physicists, Wiley, Weinheim, 2006. 5258

Tulaczyk, S., Kamb, B., Scherer, R., and Engelhardt, H.: Sedimentary processes at the base of a West Antarctic ice stream: constraints from textural and compositional properties of subglacial debris, J. Sediment Res., 68, 487–496, doi:10.2110/jsr.68.487, 1998. 5270, 5272, 5274

Tulaczyk, S., Kamb, W. B., and Engelhardt, H. F.: Basal mechanics of ice stream B, West Antarctica: 1. Till mechanics, J. Geophys. Res., 105, 463–481, doi:10.1029/1999JB900329, 2000. 5266

Walter, J. I., Brodsky, E. E., Tulaczyk, S., Schwartz, S. Y., and Pettersson, R.: Transient slip events from near-field seismic and geodetic data on a glacier fault, Whillans Ice Plain, West Antarctica, J. Geophys. Res., 116, 112–120, doi:10.1029/2010JF001754, 2011. 5257

Walter, J. I., Svetlizky, I., Fineberg, J., Brodsky, E., Tulaczyk, S., Barcheck, C., and Carter, S.: Rupture speed dependence on initial stress profiles: Insights from glacier and laboratory stick-slip, Earth Planet. Sc. Lett., 411, F01021, doi:10.1016/j.epsl.2014.11.025, 2015. 5257

Whillans, I., Bolzan, J., and Shabtaie, S.: Velocity of ice streams B and C, Antarctica, J. Geophys. Res., 92, 8895–8902, 1987. 5254

Wiens, D. A., Anandakrishnan, S., Winberry, J. P., and King, M. A.: Simultaneous teleseismic and geodetic observations of the stick–slip motion of an Antarctic ice stream, Nature, 453, 770–774, 2008. 5255

Willis, J.: Interfacial stresses induced by arbitrary loading of dissimilar elastic half-spaces joined over a circular region, IMA J. Appl. Math., 7, 179–197, 1971. 5264

Winberry, J., Anandakrishnan, S., and Alley, R.: Seismic observations of transient subglacial water-flow beneath MacAyeal Ice Stream, West Antarctica, Geophys. Res. Lett., 36, 11502, doi:10.1029/2009GL037730, 2009. 5274

TCD
9, 5253–5289, 2015

Winberry, J., Anandakrishnan, S., Wiens, D., and Alley, R.: Nucleation and seismic tremor associated with the glacial earthquakes of Whillans Ice Stream, Antarctica, Geophys. Res. Lett., 40, 312–315, doi:10.1002/grl.50130, 2013. 5255, 5257, 5259, 5261, 5274

Winberry, J. P., Anandakrishnan, S., and Wiens, D.: Whillans Stick-slip 2010, GPS Data Set, UNAVCO, Boulder, Colorado, doi:10.7283/T5XG9PFJ, 2014a. 5256, 5276

Winberry, J. P., Anandakrishnan, S., and Wiens, D.: Whillans Stick-slip 2011, GPS Data Set, UNAVCO, Boulder, Colorado, doi:10.7283/T5SQ8XPC, 2014b. 5256, 5276

Winberry, J. P., Anandakrishnan, S., Alley, R. B., Wiens, D. A., and Pratt, M. J.: Tidal pacing, skipped slips and the slowdown of Whillans Ice Stream, Antarctica, J. Glaciol., 60, 795–807, 2014c. 5255, 5256, 5257, 5274, 5275

Wittlinger, G. and Farra, V.: Observation of low shear wave velocity at the base of the polar ice sheets: evidence for enhanced anisotropy, Geophys. J. Int., 190, 391–405, 2012. 5262

Zoet, L., Carpenter, B., Scuderi, M., Alley, R., Anandakrishnan, S., Marone, C., and Jackson, M.: The effects of entrained debris on the basal sliding stability of a glacier, J. Geophys. Res., 118, 656–666, doi:10.1002/jgrf.20052, 2013. 5266, 5268

TCD
9, 5253–5289, 2015

Table 1. Table of material properties that are held fixed.

Quantity	Symbol	Unit	Value
Ice shear modulus	G_i	MPa	3664
Ice density	ρ_i	$kg\,m^{-3}$	916
Ice Poisson ratio	ν_i		0.33
Ice quality factor	Q		750
Ice wave speed	c_i	$m\,s^{-1}$	2000
Ice thickness	H	m	800 m
Bed density	ρ_b	$kg\,m^{-3}$	1700
Bed Poisson ratio	ν_i		0.49
Nominal friction coefficient	f_0		0.4
Nominal sliding velocity	V_0	$m\,s^{-1}$	10^{-5}
State evolution distance	L	m	10^{-6}
Direct effect parameter	a		5×10^{-3}
Healing parameter	b		15×10^{-3}
Maximum observed sliding velocity	V_{max}	$m\,s^{-1}$	7.47×10^{-4}

TCD
9, 5253–5289, 2015

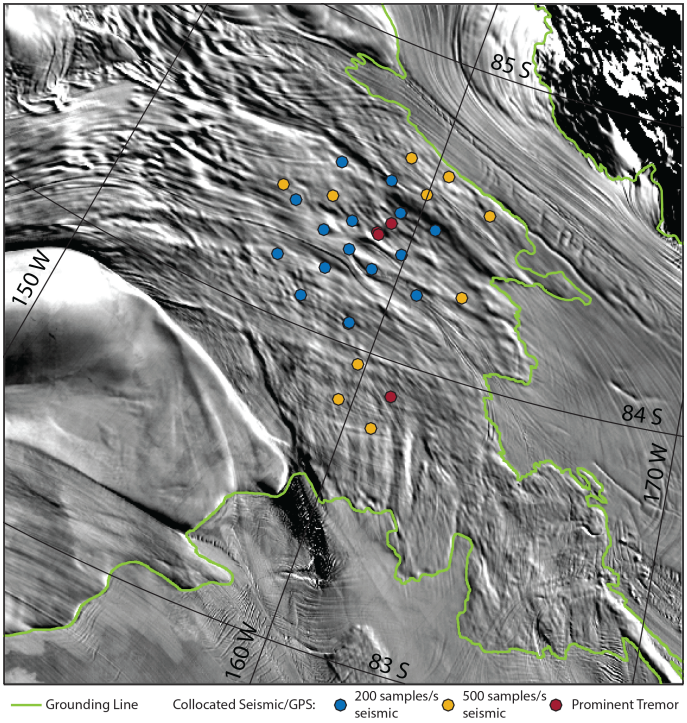

Figure 1. Map of the Whillans Ice Plain (WIP) and surrounding area. The dots show the collocated seismometer-GPS deployments used in this study. The yellow dots indicate the locations of seismometers recording at 500 Hz, the blue dots indicate the locations of seismometers recording at 200 Hz, and the red dots show the location of the seismometers that most clearly record the tremor signal. The northern- and southern-most red dots shows stations that recorded at 500 Hz; the third red dot shows the important 200 Hz station BB09. The grounding line is shown in green. The greyscale background is from the MODIS composite image of Antarctica (Scambos et al., 2007; Haran et al., 2014).

TCD
9, 5253–5289, 2015

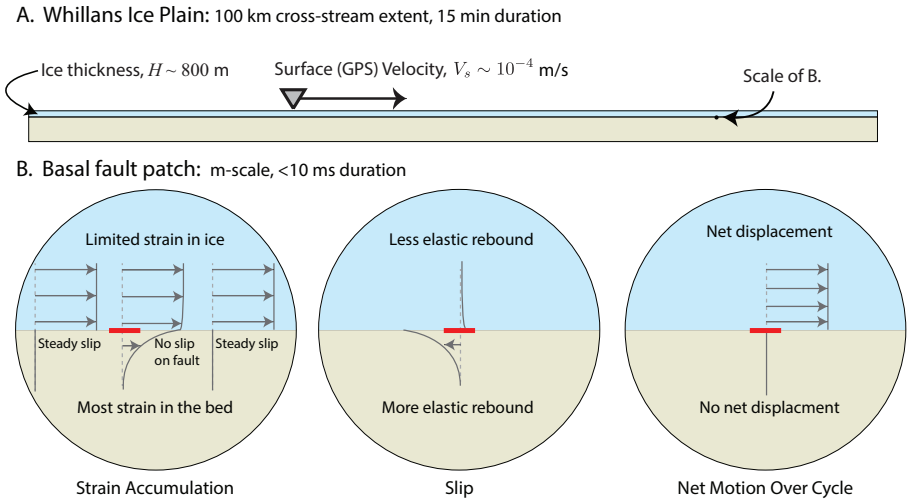

Figure 2. Schematic illustration showing the two different spatial and temporal scales of stick slip motion in the Whillans Ice Plain (WIP). **(a)** The entirety of the WIP undergoes stick slip motion with 100 km extent. During this time the ice slides with elevated velocity for approximately 15 min duration. **(b)** During large-scale sliding, small repeating earthquakes happen with duration less than 10 ms on fault patches several meters in radius. Through our analysis we infer a compliant bed which implies that more motion occurs in the till than in the ice at the scale of the tremor patch.

TCD
9, 5253–5289, 2015

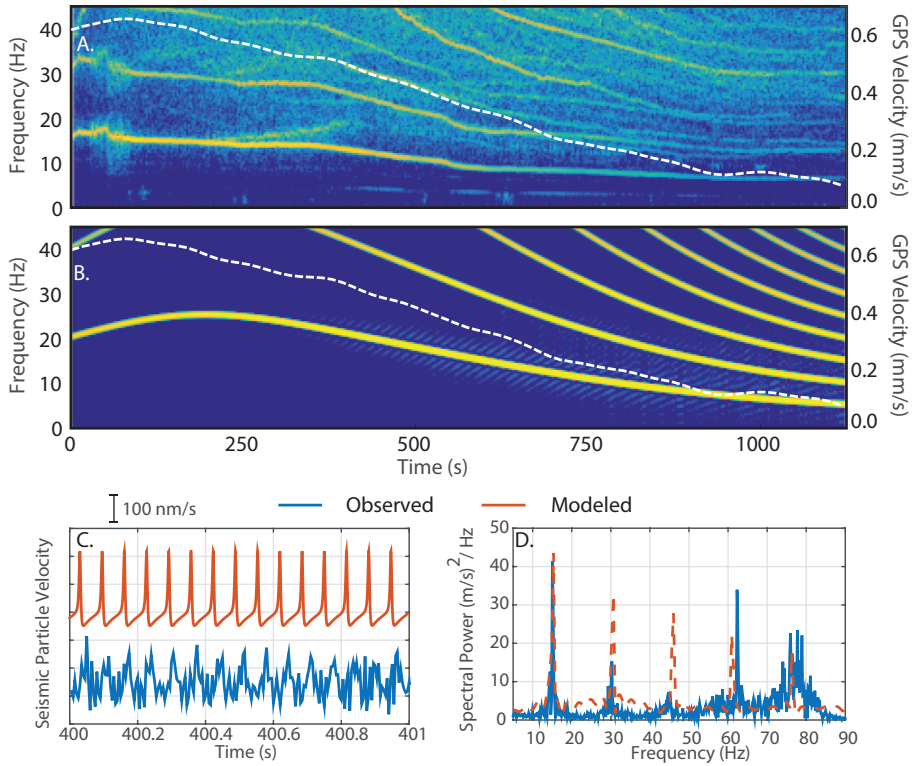

Figure 3. Comparison between observed **(a)** and modeled **(b)** tremor episode spectrograms for the episode that occurred on 14 January 2011 at 11:31 LT. The logarithmic color scales in both spectrograms are the same and have units of power spectral amplitude $(\mathrm{m\,s^{-1}})^2\,\mathrm{Hz^{-1}}$. The data were high pass filtered above 1 Hz before creating the spectrograms. The spectrograms use an 800 sample window with 50 % overlap. We compare the modeled (red) and observed (blue) seismic velocity trace in **(c)** and frequency spectrum in **(d)**. The frequency spectrum in **(d)** is calculated over four second time windows for both the data and the model.

TCD
9, 5253–5289, 2015

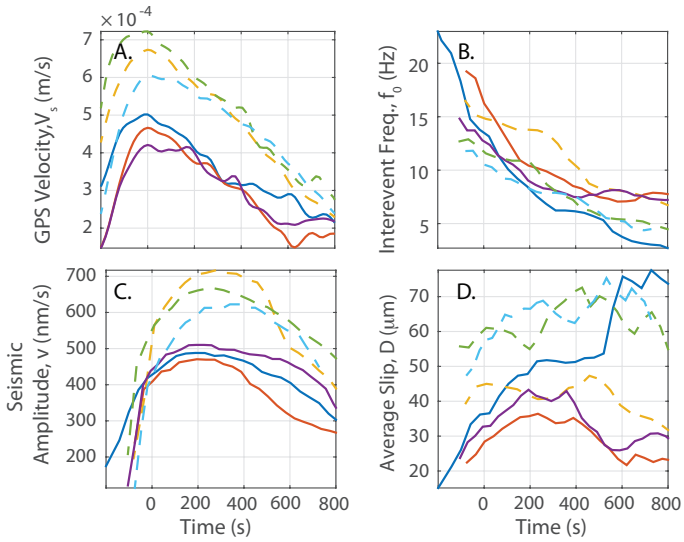

E.

Color	Date	Time	Tide (m)	Wait Time (h)
	2011-01-01	14:40	+0.66	16.47
	2011-01-12	22:49	-0.65	12.53
	2011-01-14	11:31	+0.60	23.43
	2011-01-14	21:20	-0.66	09.82
	2011-01-19*	15:45	+0.77	24.83
	2011-01-26*	12:26	+0.22	22.21

Figure 4. Attribute time series for six tremor episodes. Events with wait times greater than 17 h are shown with dashed lines and events with wait times less than 17 h are shown with solid lines. Surface velocities **(a)** are positively correlated with the waiting time between large-scale sliding events, as shown in the table **(e)**. Slip per event **(d)** is calculated using Eq. (3) which takes as inputs tremor frequency **(b)** the GPS-recorded surface velocity **(a)**. **(c)** shows the seismometer-recorded particle velocity amplitude envelope. Collocated GPS data was not available at BB09 for the events marked with asterisks; data were used from the station BB02 for these events.

TCD
9, 5253–5289, 2015

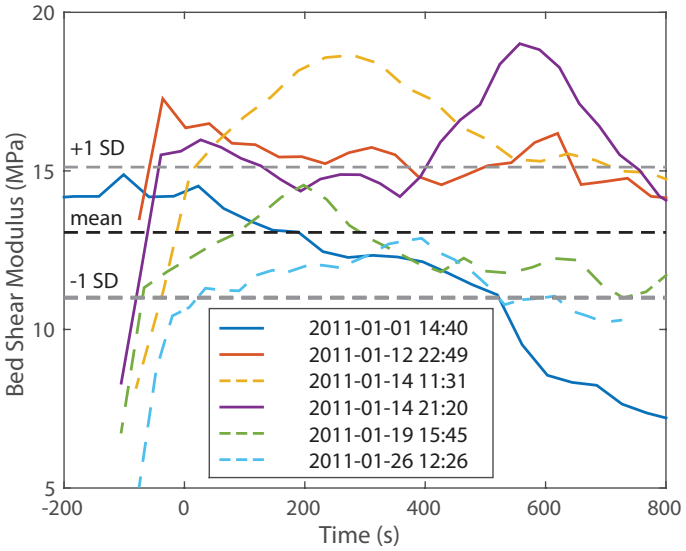

Figure 5. Time series of the inferred bed shear modulus, G_b, for six tremor episodes. See the table in Fig. 4e for information about these events. Events with wait times greater than 17 h are shown with dashed lines, and events with wait times less than 17 h are shown with solid lines. The bed shear modulus is calculated using Eq. (21). The horizontal dashed black line is the mean over all events and times and the horizontal dashed grey lines are the one standard deviation bounds.

TCD
9, 5253–5289, 2015

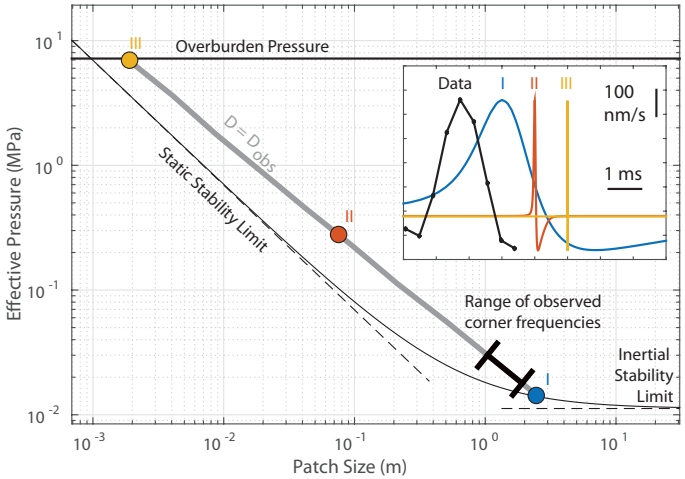

Figure 6. A diagram showing the range of patch size-effective pressure $R - \bar{\sigma}$ conditions that give rise to fault slip $D_{obs} = 25\,\mu m\,s^{-1}$ (thick grey line). The heavy black line shows the subset of parameter space that is also consistent with observed corner frequencies. The fault is loaded with velocity $V_s = 0.4\,mm\,s^{-1}$. The lower thin curve shows the boundary of the stability region Eq. (19). The horizontal line shows the overburden stress $\rho_i g H$. The inset shows a representative wave pulse recorded at high rate at station GS07 on 14 December 2010 as compared to three simulated wave forms. The bed shear modulus G_b for the simulations is chosen from Fig. 5 to be 15 MPa. Each simulation has the same seismic amplitude and slip; they differ only corner frequency ($f_c \approx 30$, 750, and 4000 Hz).

TCD
9, 5253–5289, 2015